









# FAST Observations of an Extremely Active Episode of FRB 20201124A. III. Polarimetry

Jin-Chen Jiang<sup>1,2</sup> , Wei-Yang Wang<sup>1,3</sup>, Heng Xu<sup>1,2,3</sup>, Jiang-Wei Xu<sup>1,2,3</sup>, Chun-Feng Zhang<sup>1,2,3</sup>, Bo-Jun Wang<sup>1,2,3</sup>,  
De-Jiang Zhou<sup>2,4</sup> , Yong-Kun Zhang<sup>2,4</sup> , Jia-Rui Niu<sup>2,4</sup> , Ke-Jia Lee<sup>1,2,3</sup>, Bing Zhang<sup>5</sup>, Jin-Lin Han<sup>2,4,6</sup>, Di Li<sup>2,4,7,8</sup>,  
Wei-Wei Zhu<sup>2</sup>, Zi-Gao Dai<sup>9</sup>, Yi Feng<sup>7</sup>, Wei-Cong Jing<sup>2,4</sup> , Dong-Zi Li<sup>10</sup>, Rui Luo<sup>11</sup> , Chen-Chen Miao<sup>2,4</sup>, Chen-Hui Niu<sup>2</sup>,  
Chao-Wei Tsai<sup>2</sup>, Fa-Yin Wang<sup>12,13</sup>, Pei Wang<sup>2</sup>, Ren-Xin Xu<sup>1,3</sup>, Yuan-Pei Yang<sup>14</sup>, Zong-Lin Yang<sup>2,4</sup>, Ju-Mei Yao<sup>15</sup>, and  
Mao Yuan<sup>2,4</sup>

<sup>1</sup> Department of Astronomy, Peking University, Beijing 100871, China; [jiangjincheng@pku.edu.cn](mailto:jiangjincheng@pku.edu.cn)

<sup>2</sup> National Astronomical Observatories, Chinese Academy of Sciences, Beijing 100101, China

<sup>3</sup> Kavli Institute for Astronomy and Astrophysics, Peking University, Beijing 100871, China

<sup>4</sup> School of Astronomy, University of Chinese Academy of Sciences, Beijing 100049, China

<sup>5</sup> Department of Physics and Astronomy, University of Nevada, Las Vegas, NV 89154, USA; [bing.zhang@unlv.edu](mailto:bing.zhang@unlv.edu)

<sup>6</sup> CAS Key Laboratory of FAST, NAOC, Chinese Academy of Sciences, Beijing 100101, China

<sup>7</sup> Research Center for Intelligent Computing Platforms, Zhejiang Laboratory, Hangzhou 311100, China

<sup>8</sup> NAOC-UKZN Computational Astrophysics Centre, University of KwaZulu-Natal, Durban 4000, South Africa

<sup>9</sup> Department of Astronomy, University of Science and Technology of China, Hefei 230026, China

<sup>10</sup> Cahill Center for Astronomy and Astrophysics, MC 249-17, California Institute of Technology, Pasadena, CA 91125, USA

<sup>11</sup> CSIRO Space and Astronomy, P.O. Box 76, Epping, NSW 1710, Australia

<sup>12</sup> School of Astronomy and Space Science, Nanjing University, Nanjing 210093, China

<sup>13</sup> Key Laboratory of Modern Astronomy and Astrophysics (Nanjing University), Ministry of Education, China

<sup>14</sup> South-Western Institute For Astronomy Research, Yunnan University, Yunnan 650504, China

<sup>15</sup> Xinjiang Astronomical Observatory, Chinese Academy of Sciences, Urumqi 830011, China

Received 2022 June 30; revised 2022 September 17; accepted 2022 October 7; published 2022 November 30

## Abstract

As the third paper in the multiple-part series, we report the statistical properties of radio bursts detected from the repeating fast radio burst (FRB) source FRB 20201124A with the Five-hundred-meter Aperture Spherical radio Telescope during an extremely active episode between the 25th and 28th of September 2021 (UT). We focus on the polarization properties of 536 bright bursts with  $S/N > 50$ . We found that the Faraday rotation measures (RMs) monotonically dropped from  $-579$  to  $-605 \text{ rad m}^{-2}$  in the 4 day window. The RM values were compatible with the values ( $-300$  to  $-900 \text{ rad m}^{-2}$ ) reported 4 months ago. However, the RM evolution rate in the current observation window was at least an order of magnitude smaller than the one ( $\sim 500 \text{ rad m}^{-2} \text{ day}^{-1}$ ) previously reported during the rapid RM-variation phase, but is still higher than the one ( $\leq 1 \text{ rad m}^{-2} \text{ day}^{-1}$ ) during the later RM no-evolution phase. The bursts of FRB 20201124A were highly polarized with the total degree of polarization (circular plus linear) greater than 90% for more than 90% of all bursts. The distribution of linear polarization position angles (PAs), degree of linear polarization ( $L/I$ ) and degree of circular polarization ( $V/I$ ) can be characterized with unimodal distribution functions. During the observation window, the distributions became wider with time, i.e., with larger scatter, but the centroids of the distribution functions remained nearly constant. For individual bursts, significant PA variations (confidence level  $5\sigma$ ) were observed in 33% of all bursts. The polarization of single pulses seems to follow certain complex trajectories on the Poincaré sphere, which may shed light on the radiation mechanism at the source or the plasma properties along the path of FRB propagation.

*Key words:* (stars:) pulsars: general – stars: magnetars – radio continuum: general – polarization

## 1. Introduction

Radio bursts from a large fraction of fast radio bursts (FRBs) are polarized. The polarization properties of nine FRB repeaters have been reported, viz. FRBs 20121102A, 20180301A, 20180916B, 20190303A, 20190417A, 20190520B, 20190604A, 20190711A and 20201124A. In general, the radio burst emission is linear polarization dominated. No significant circular polarization has been detected except for FRB 20190520B (Anna-Thomas et al. 2022; Dai et al. 2022) and FRB

20201124A (Hilmarsson et al. 2021b; Kumar et al. 2022b; Xu et al. 2022).

FRB 20121102A is the most intensively studied FRB repeater. It was discovered with the Arecibo Telescope (Spitler et al. 2014), and later confirmed to be a repeater (Spitler et al. 2016). Its bursts are  $\sim 100\%$  linearly polarized with flat position angle (PA) curves as measured in the C-band (Gajjar et al. 2018; Michilli et al. 2018). However, the degree of linear polarization becomes significantly smaller in the L-band (Li et al. 2021; Feng et al. 2022;

Plavin et al. 2022). The Faraday rotation measure (RM) of FRB 20121102A ( $\sim 10^5 \text{ rad m}^{-2}$ ) is much larger than that of other FRBs, which showed a long-term decreasing trend and short-term variations (Gajjar et al. 2018; Michilli et al. 2018; Faber et al. 2021; Hilmarsson et al. 2021a).

FRB 20180301A was discovered by the Parkes ‘‘Murriyang’’ radio telescope (Price et al. 2019), and was confirmed to be a repeater with the Five-hundred-meter Aperture Spherical radio Telescope (FAST) follow-up observations (Luo et al. 2020). Its bursts were linearly polarized but the degrees of linear polarization could be significantly less than 100%, and the PA could be either constant or varying across individual bursts (Luo et al. 2020; Feng et al. 2022).

FRB 20180916B was discovered by the Canadian Hydrogen Intensity Mapping Experiment (CHIME) (CHIME/FRB Collaboration et al. 2019). Its bursts are also  $\sim 100\%$  linearly polarized above 300 MHz with flat PA curves (CHIME/FRB Collaboration et al. 2019; Chawla et al. 2020; Nimmo et al. 2021; Pastor-Marazuela et al. 2021; Sand et al. 2022). The degree of linear polarization decreases to 30%–70% at 110–188 MHz (Pleunis et al. 2021).

FRB 20190520B was discovered with FAST (Niu et al. 2022). Most of its detected bursts are linearly polarized with the degree of linear polarization ranging from 15% to 80% (Anna-Thomas et al. 2022; Dai et al. 2022). A single incidence of FRB 20190520B exhibited  $(42 \pm 7)\%$  circular polarization (Anna-Thomas et al. 2022).

FRB 20190711A was discovered by the Australian Square Kilometre Array Pathfinder (ASKAP) with  $\sim 100\%$  linear polarization and flat PA curves (Day et al. 2020). An extremely band-limited repetition detected by Parkes Telescope also showed a high degree of linear polarization (80%) and a flat PA (Kumar et al. 2021).

Repeating FRBs 20190303A, 20190417A and 20190604A were discovered by CHIME (Fonseca et al. 2020). Bursts from FRB 20190303A have been 100% linearly polarized at  $L$ -band with flat PA curves, and its RM changed by  $\sim 100 \text{ rad m}^{-2}$  in 1.5 yr (Feng et al. 2022). Bursts from FRB 20190417A have also been also linearly polarized with flat PA curves, but their degree of linear polarization ranged from 52% to 86% (Feng et al. 2022). A burst from FRB 20190604A exhibited 100% linear polarization with a flat PA curve (Fonseca et al. 2020).

In this paper, we focus on the polarization properties of FRB 20201124A. The source was discovered by CHIME. It entered a period of high activity between March and May of 2021 (CHIME/FRB Collaboration 2021; Lanman et al. 2022; Xu et al. 2022). During the active episode, the source manifested very rich polarization behaviors unprecedented among other FRB repeaters. Hilmarsson et al. (2021b) employed the Effelsberg Telescope to observe FRB 20201124A at 1.36 GHz on 2021 April 9, and obtained flat PA curves but with degrees of circular polarization up to 20%. Kumar et al. (2022b) used Parkes Telescope to observe the source and detected a burst with about 47% of circular polarization, and a change of about  $50^\circ$  in PA was also detected between its two components. The FAST observations detected 1863 bursts from the

source (Xu et al. 2022). Many interesting features were observed from this large sample of bursts: (1) both PA swings and flat PA profiles are found from the bursts; (2) high degrees of circular polarization up to 75.1% have been detected in a fraction of the bursts; and (3) apparent oscillations between linear and circular polarizations are observed in some bursts.

As the third paper in the multiple-part series, this paper reports the polarization properties of FRB 20201124A observed in its active window between the 25th and 28th of September 2021 (UT). The current paper is organized as follows. We describe the setups of our observation in Section 2. In Section 3 the data reduction procedures are explained. The results of all detected bursts are shown and discussed in Section 4 and conclusions are drawn in Section 5. The burst morphology, energetic statistics and timing results for the same set of data are reported in companion papers Zhou et al. (2022, Paper I), Zhang et al. (2022, Paper II) and Niu et al. (2022, Paper IV) respectively.

## 2. Observation

We observed FRB 20201124A with FAST using the central beam of the 19-beam receiver (Dunning et al. 2017; Li et al. 2018; Jiang et al. 2019, 2020). The source was observed daily between 2021 September 25 and 28 (UT). The length of each observing session was approximately one hour, and the starting epochs (in MJD) of the four sessions were 59482.942361, 59483.861806, 59484.813194 and 59485.781944, respectively. FAST was pointed to the coordinate provided by the European VLBI Network (EVN), i.e.,  $R. A. = 05^h 08^m 03^s.5077$ ,  $decl. = +26^\circ 03' 38'' 504$  (Marcote et al. 2021; Nimmo et al. 2022). At the beginning and end of each observation, 1 minute noise signals were injected for the purpose of polarization calibration (see Section 3.2). We sampled the raw voltage using a ROACH2-board based digital backend (Jiang et al. 2019, 2020), which recorded the search-mode filterbank data in 8-bit PSRFITS format (Hotan et al. 2004). We recorded the full coherency matrix, and later converted into the 4-channel Stokes-parameters format. For the full bandwidth of 1.0–1.5 GHz, our frequency resolution was 4096 channels  $\times$  122 kHz, and the time resolution was 49.152  $\mu\text{s}$ .

## 3. Data Reduction

### 3.1. FRB Searching

We used the software package `TransientX`<sup>16</sup> to search off-line for FRB bursts in the data. For FRB 20201124A, the dispersion measure (DM) and DM fluctuation had been known ( $DM \sim 410 \text{ pc cm}^{-3}$  with  $\Delta DM \sim 10 \text{ pc cm}^{-3}$ , CHIME/FRB Collaboration 2021; Xu et al. 2022), so we set the DM search scheme to have a uniform grid, for which the DM step is  $0.1 \text{ pc cm}^{-3}$  and the DM range is 405–420  $\text{pc cm}^{-3}$ . Burst signals were searched using the matched filters with an equal-

<sup>16</sup> <https://github.com/ypmen/TransientX>

SNR-loss grid of time widths ranging from 0.1 to 100 ms (Men et al. 2019);  $2 \times 20$  MHz bandpass edges were removed on both sides to avoid the aliasing effect. Following the community convention (Zhang et al. 2021), the detection threshold of signal-to-noise ratio (S/N) is chosen to be 7. All the search candidates were later verified by eye to exclude radio frequency interference (RFI) contamination, despite a significant amount of RFI being automatically mitigated with `TransientX` using algorithms described in Men et al. (2019).

As discussed in Paper I, the estimation of DM could be affected by the distorted pulse pattern for individual bursts with multi-peak or drifting morphology. Examining DMs of bursts with multiple components showed no systematic variations in the timescale of one hour. Therefore, after the burst detection, we re-performed dedispersion using the average DM of each observation in Table 1 of Paper I, i.e., the daily average DMs are  $DM_{\text{mean}} = 412.38, 412.25, 412.53$  and  $411.56 \text{ cm}^{-3} \text{ pc}$ , respectively, from September 25 to 28.

Barycentric burst times were converted from topocentric times using `TEMPO2`<sup>17</sup> (Hobbs et al. 2006; Hobbs 2012; Hobbs & Edwards 2012). Barycentric burst times are in Barycentric Coordinate Time (TCB), and the reference frequency is 1.5 GHz.

In the following polarization analysis, we raised the threshold of S/N to 50. There are two major reasons. On one hand, we need to channelize the data to measure the PA rotation as a function of frequency to get RM. The S/N per channel is lower than that of the full band. In this way, RM can be only measured reliably with high S/N data. On the other hand, we need a good S/N in polarization intensity. The degree of polarization could be low (a few percent) for some bursts, which further forces us to raise the S/N threshold of selecting bursts in the polarization analysis. The threshold of  $S/N \geq 50$  cuts down the numbers of bursts to 15, 39, 153 and 329 on the days of MJD 59482 to 59485, respectively. The numbers of bursts included in our analysis are, thus, different from other papers in this series of papers on FAST observations of FRB 20201124A.

### 3.2. Polarimetric Calibration

The 19-beam receiver of FAST uses orthogonal linear polarization feeds. At the beginning and the end of each observation, wide-band noise diode signals were injected as the  $45^\circ$  100% linearly polarized calibrator signal. The noise signals were amplitude modulated with a periodic square wave, whose period and duty cycle were 0.201326592 s and 50%, respectively. We applied the software package `DSPSR`<sup>18</sup> (van Straten & Bailes 2011) to fold the calibration files, and used the single-axial model of software package `PSRCHIVE`<sup>19</sup> (Hotan et al. 2004; van Straten et al. 2012) for polarimetric calibration. In this manuscript, we follow the PSR/IEEE

convention (van Straten et al. 2010) for the definition of Stokes parameters, where the total intensity is denoted as  $I$ , the two linear parameters as  $Q, U$ , and the circular component as  $V$ . Our polarization presentation on the Poincaré sphere is defined by

$$Q = P \cos 2\chi \cos 2\Psi, \quad (1)$$

$$U = P \cos 2\chi \sin 2\Psi, \quad (2)$$

$$V = P \sin 2\chi, \quad (3)$$

where  $\Psi$  is the linear position angle (PA) and  $\chi$  is the ellipticity angle. The total polarization intensity is  $P = \sqrt{Q^2 + U^2 + V^2}$ .

Part of the observations on September 27 and 28 (MJD 59484 and 59484) entered the large zenith angle ( $>26^\circ.4$ ), beyond which the effective reflector is not axisymmetric. We have evaluated how such a large zenith angle illumination affects the polarimetry of FAST, the details of which are presented in Appendix A.

It turns out that the algebraic operations of computing the linear and total polarization using the Stokes parameters leads to statistical biases. Thus, after the polarization calibration, we perform the generalized Weisberg correction (Everett & Weisberg 2001) before computing the linear and total polarization intensities, which are defined as  $L = \sqrt{Q^2 + U^2}$  and  $P = \sqrt{Q^2 + U^2 + V^2}$  respectively. The Weisberg correction modifies the algebraic operation to

$$L_{\text{true}} = \sqrt{\sum_{i=1,2} S_i^2 - \varepsilon_L}, \quad (4)$$

$$P_{\text{true}} = \sqrt{\sum_{i=1,2,3} S_i^2 - \varepsilon_P}, \quad (5)$$

where  $S_1 = Q, S_2 = U$  and  $S_3 = V$ . The subscript is introduced to shorten the notation. The corrections are

$$\varepsilon_L = \frac{\sum_{p(1,2)} S_{p(i)}^2 \sigma_{p(j)}^2}{\sum_{i=1,2} S_i^2}, \quad (6)$$

$$\varepsilon_P = \frac{\sum_{p(1,2,3)} (S_{p(i)}^2 + S_{p(j)}^2) \sigma_{p(k)}^2}{\sum_{i=1,2,3} S_i^2}, \quad (7)$$

where  $\sum_{p(i,j)}$  or  $\sum_{p(i,j,k)}$  perform summation over all possible permutations of indices  $i, j$  or  $i, j, k$  respectively.

### 3.3. Absolute Flux Determination

We estimate the burst flux from the S/N, as no flux calibrator was arranged to save the telescope time. The expected mean flux  $S$  is computed from radiometer equation

$$S_\nu = \frac{T_{\text{sys}}(S/N)}{G\sqrt{2B\tau}}, \quad (8)$$

where  $T_{\text{sys}}$  is the effective system temperature,  $G$  is the effective gain of the telescope,  $B$  is the bandwidth used for detection and  $\tau$  is the integration time. The factor 2 comes from combining the two orthogonal polarizations. Here, the system efficiency is already included in the effective gain and system

<sup>17</sup> <https://bitbucket.org/psrsoft/tempo2/>

<sup>18</sup> <http://dsp.sr.sourceforge.net>

<sup>19</sup> <http://psrchive.sourceforge.net>

temperature. The specific fluence ( $F_\nu$ ) was then derived by integrating the specific flux over the pulse width of the FRB burst,

$$F_\nu = \int_{t_0}^{t_1} S_\nu(\nu, t) dt, \quad (9)$$

where  $t_1 - t_0$  is pulse width. The mean fluence ( $F$ ) is the average value of fluence over the pulse signal bandwidth (i.e.,  $B = \int_{f_1}^{f_2} d\nu$ , see Xu et al. 2022 for the details of bandwidth definition) such that

$$F = \frac{1}{B} \int_{f_1}^{f_2} F_\nu d\nu, \quad (10)$$

with which the burst energy ( $E$ ) becomes

$$E = \frac{4\pi D_L^2}{1+z} FB, \quad (11)$$

where  $D_L = 453.3$  Mpc is the luminosity distance of FRB 20201124A. We used the redshift  $z = 0.09795$  measured by Xu et al. (2022).

In the above estimation for the absolute flux, the *observed bandwidth* of burst signal is defined within the observing frequency window, i.e., 1–1.5 GHz. However, the *intrinsic bandwidth* could extend beyond the observing window. Thus, a Gaussian fitting method (Xu et al. 2022) is utilized to estimate intrinsic bandwidths, which are shown in Figures 1, 3 and F4.

#### 4. Results and Discussions

We adopt nine different parameters to characterize the polarization properties of the bursts from FRB 20201124A. The parameters are (1) RM, (2) mean PA  $\Psi$ , (3) maximum change in the PA across the pulse profile  $\Delta\Psi$ , (4) the maximum change in the ellipticity angle across the pulse profile  $\Delta\chi$ , (5) average degree of linear polarization  $L/I$ , (6) average degree of circular polarization  $V/I$ , (7) average degree of total polarization  $P/I$ , (8) burst energy  $E$  and (9) burst bandwidth  $B$  using Gaussian fitting. The methods to measure  $L/I$ ,  $V/I$ ,  $P/I$ ,  $E$  and  $B$  are described in Sections 3.2, 3.3. The definition and inference of the rest of the parameters are lengthy and technical, which are summarized in Appendices B–E for readers' reference.

The daily distribution of burst properties is displayed in Figure 1 and the related statistics are reported in Table 1. The distributions in Figure 1 are presented using violin plots, where the curve of each epoch shows the distribution function of measured values. The density is estimated using the Gaussian kernel method implemented in `scikitlearn`<sup>20</sup> (Pedregosa et al. 2011). The *most probable* values (the values at which the distribution density is maximal) of all parameters exhibit no

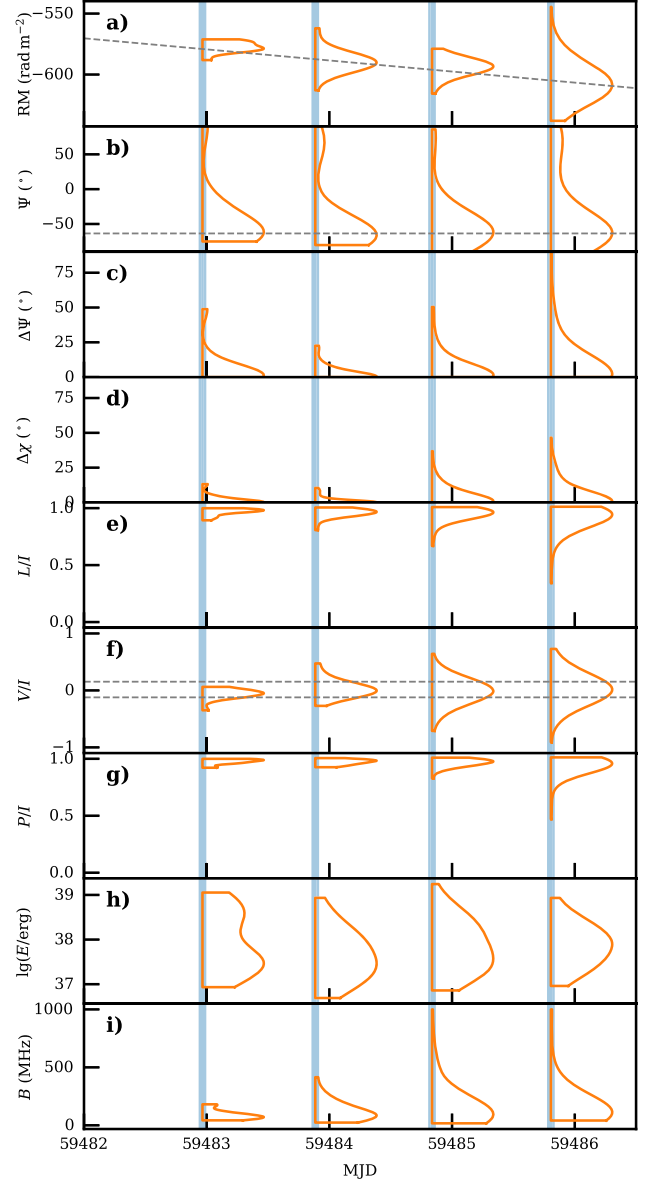


**Figure 1.** Violin plots (orange lines) of the polarization properties of the bursts. (a) RM of interstellar and intergalactic media after subtracting the contribution of the ionosphere of the Earth. The dashed gray line is the fitting of a linear model, as a function of time, to all the measured RM values. (b) Mean PA  $\Psi$  of the bursts, corrected to infinite frequency. The dashed gray line signifies the averaged value of the PA weighted by burst energy. (c) Maximum change of PA  $\Psi$  in each burst. (d) Maximum change of ellipticity angle  $\chi$  in each burst. (e) Degree of linear polarization  $L/I$  after correcting for Faraday rotation. (f) Degree of circular polarization  $V/I$ . The two dashed gray lines mark the 68% interval of the distribution across the four days. (g) Degree of polarization  $P/I$ . (h) Burst energy  $E$  in the observed bandwidth. (i) Burst bandwidth  $B$  in the observed bandwidth. The vertical blue spans represent the observing time ranges.

significant changes except for the RM. The RMs after subtracting the contribution of the Earth's ionosphere showed a decreasing rate of  $(-9.3 \pm 0.5)$   $\text{rad m}^{-2} \text{day}^{-1}$  by linearly fitting the value of each burst. After subtracting the linear variation,

<sup>20</sup> <https://scikit-learn.org/stable/modules/generated/sklearn.neighbors.KernelDensity.html>



**Table 1**  
Standard Deviations of  $\Psi$ ,  $\Delta\Psi$ ,  $\Delta\chi$ ,  $L/I$ ,  $V/I$  and  $P/I$  for the Bursts Detected on Different days

MJD	59482	59483	59484	59485
$\sigma_{\Psi}$ (°)	$18 \pm 6$	$19.2 \pm 3.5$	$19 \pm 4$	$27.1 \pm 1.6$
$\sigma_{\Delta\Psi}$ (°)	$12.2 \pm 2.2$	$5.3 \pm 0.6$	$9.6 \pm 0.6$	$13.7 \pm 0.5$
$\sigma_{\Delta\chi}$ (°)	$3.4 \pm 0.6$	$2.54 \pm 0.29$	$6.2 \pm 0.4$	$7.72 \pm 0.30$
$\sigma_{(L/I)}$	$0.029 \pm 0.005$	$0.038 \pm 0.004$	$0.0533 \pm 0.0030$	$0.0841 \pm 0.0033$
$\sigma_{(V/I)}$	$0.094 \pm 0.017$	$0.143 \pm 0.016$	$0.169 \pm 0.010$	$0.201 \pm 0.008$
$\sigma_{(P/I)}$	$0.023 \pm 0.004$	$0.0231 \pm 0.0026$	$0.0318 \pm 0.0018$	$0.0625 \pm 0.0024$

**Note.** Due to the  $\pi$  periodicity,  $\sigma_{\Psi}$  is defined with circular statistics (Fisher 1996) as explained in Appendix E. The rounding of measured values and errors in this table and other parts of the manuscript follows the rounding rules defined at <https://pdg.lbl.gov/2021/reviews/rpp2021-rev-rpp-intro.pdf#page=18>.

the Kolmogorov–Smirnov test yields  $p$ -values that are smaller than 0.05, leading to rejecting the hypothesis that any two data samples are from the same population, except for the first (MJD 59482) and the third day (MJD 59484), where  $p$ -value is 0.53. Note that the absolute value of RM, in fact, *increases* due to the fact that  $RM < 0$ . The evolution of RM over the four-day observations verifies the previous conclusion from Xu et al. (2022) that a highly variable magnetoionic environment exists around the FRB source with a spatial scale of  $0.5 \text{ au}(v/100 \text{ km s}^{-1})(\tau/10 \text{ day})$ . The daily RM scatter is increasing, as the distribution becomes wider with time. Xu et al. (2022) demonstrated that the RMs of FRB 20201124A followed the cold plasma Faraday rotation relation such that the rotation of polarization plane was proportional to the square of wavelength; and they also proved that the daily RM fluctuations were not caused by a profile evolution or apparent RM changes due to intrinsic polarization structures in pulsed signals. Therefore, we attribute the RM fluctuation to the increase of activities in the FRB local environment, where the RM fluctuation could be caused either by a larger scattering disk or a higher amplitude of plasma turbulence. We can compare the current observation with the results in May (Figure 2). One can see that the RM values were compatible with what we saw in May. The fluctuation level of daily RM was, however, higher than that in May, but was compatible with the RM fluctuation level seen in March to April (Xu et al. 2022). Clearly, certain mechanisms that alter the plasma properties of the FRB environment on the timescale of a month are expected.

We point out the similarities between the distributions of single burst polarization properties from FRB 20201124A and of the polarization properties of pulsar single pulses. As noted by Stinebring et al. (1984), the pulsar single pulses are highly fluctuating in terms of their polarization properties. Individual pulses can reach a high degree of polarization, despite the integrated pulse profiles showing a low degree of polarization. We see similar properties in FRB 20201124A: the individual burst polarization is also highly fluctuating and the tails in the distributions of  $L/I$  and  $V/I$  can both extend to extreme values from non-polarized to nearly 100% fully polarized. However, since we do not find a spin-like period here (see Paper IV, Niu et al. 2022), we cannot further study the phase dependent polarization properties at this stage.

The PA ( $\Psi$ ) traces the geometry of the magnetic field lines in the FRB emission region, as the linear polarization plane is determined by the local magnetic field direction for either the coherent bunched radiation from magnetosphere (Kumar & Bošnjak 2020; Lu et al. 2020; Wang et al. 2020, 2022b; Yang & Zhang 2021; Wang et al. 2022b; Zhang 2022) or the synchrotron maser mechanism from magnetic, relativistic shocks far outside the magnetospheres (Metzger et al. 2019; Beloborodov 2020; Margalit et al. 2020). We note that the most probable value of the PAs stayed constant, in contrast to what we have seen in RM. In this way, we expect that the geometry of magnetic field lines in the emission region has been maintained with similar configurations in the four-day observation window. This agrees with either picture of the FRB emission region. In the former picture, the geometry is fixed by the strong magnetic fields in the magnetosphere, whereas in the shock wave picture, an upstream ordered magnetic field provides the fixed direction. The overall stable magnetic field structure in emission region is further confirmed by the stability of other polarization related parameters, including  $\Delta\chi$ ,  $\Delta\Psi$ ,  $L/I$ ,  $V/I$  and  $P/I$ .

On the other hand, the daily standard deviations (i.e., widths of distribution) of  $\Psi$ ,  $\Delta\Psi$ ,  $\Delta\chi$ ,  $L/I$ ,  $V/I$  and  $P/I$  evolved significantly (more than  $5\sigma$ ) in the four-day observations (see the related numbers in Table 1). These effects do not come from the artifacts caused by the increasing number of detected bursts. In particular, in MJD 59484 and 59485, the numbers of daily detected bursts are more than 150. The statistical fluctuation should introduce errors less than 8%, which are smaller than the changes in the distribution widths. In the magnetospheric models, the evolution in the distribution width of  $\Psi$  indicates that the size of emission region varied such that a variable range of  $\Psi$  was covered.

The current observation showed higher degrees of linear and total polarization compared to what we saw in March to May. The average degrees of linear and total polarization of the current observations were  $L/I = (95.8 \pm 0.6)\%$  and  $P/L = (97.0 \pm 0.5)\%$ , respectively, while the corresponding values for the March to May observation were,  $(83.4 \pm 2.3)\%$  and  $(85.4 \pm 1.8)\%$ , respectively. The average degree of circular polarization agrees with

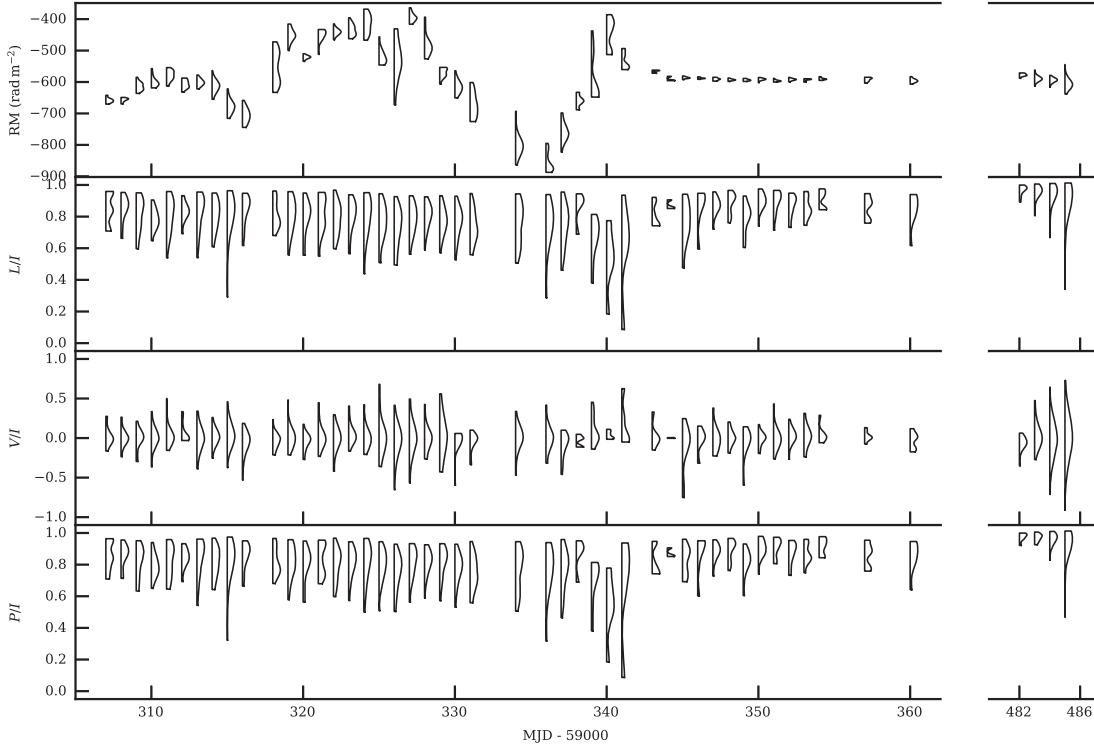


**Figure 2.** Comparison of RM between observations in March to May and in September, 2021. The results between March and May were in Xu et al. (2022).

0, where  $V/I = (-0.5 \pm 1.0)\%$  and  $(-1.4 \pm 1.8)\%$  in the current and the March-to-May observation session, respectively. The distribution of  $V/I$ ,  $L/I$  and  $P/I$  also evolved to a more scattered state during the current observation as affirmed in Figure 1. Such an evolution was not detected in the previous observation (Xu et al. 2022) as shown in Figure 2, where the standard deviations of the distribution functions of polarization degrees are nearly constant, except the possible jitter around 2021 May 6 (MJD 59340).

As the distribution of circular polarization became more spread out, approximately 0.6% of bursts in the current observation session had degrees of circular polarization higher than 70%. Considering the intrinsic mechanisms, such a high degree of circular polarization can be produced via the off-beam curvature radiation from bunches (Wang et al. 2022a), but cannot be achieved for the synchrotron maser mechanism. Propagation effects can also generate circular polarization through two possible channels: (1) the polarization dependent radiative transferring (Xu et al. 2022), or (2) multi-path propagation (Beniamini et al. 2022; Feng et al. 2022; Yang et al. 2022). We can neither exclude the intrinsic mechanism nor propagation effects at this stage, because the off-beam curvature radiation can be a natural consequence of an extended radiation region indicated by the scattering of  $\Psi$ ; the propagation mechanisms are supported by the detected polarization oscillations (Xu et al. 2022); and the multi-path

propagation may be supported by the increase of the scatter in the RM distribution.

Significant ( $>5\sigma$ ) variations of the PA across pulse profile ( $\Delta\Psi$ ) were detected in 33% of the high S/N bursts with  $S/N > 50$ , while variations of ellipticity angle ( $\Delta\chi$ ) were detected in 28% of the high S/N bursts. The distribution of  $\Delta\chi$  and  $\Delta\Psi$  grew wider in the current four-day observation. In the magnetospheric models, variation in distribution width of  $\Delta\Psi$  and  $\Delta\chi$  can be well understood, if the geometric size of emission region is not stationary as already noticed in the case of pulsars (Stinebring et al. 1984). However, for the shock model, the nonzero values of  $\Delta\Psi$  require a fine-tuned magnetic field configuration to create the swing of polarization plane during several milliseconds. The nonzero values of  $\Delta\chi$  indicate that the degree of circular polarization changes within the bursts, which could be the consequence when combining nonzero  $\Delta\Psi$  and polarization-dependent radiative transferring (Huang & Shcherbakov 2011).

The distribution functions of energy and signal bandwidth seem to be constant. The 19-beam receiver limits the total bandwidth to 460 MHz (with 20 MHz bandedge removed on each side). Such an instrumental limitation introduces artificially sharp cutoffs in the energy distributions in Figure 1. The widths of either the bandwidth or the energy distribution are wide, and that of the burst energies spans more than two orders of magnitude. Due to the wide widths of the distributions, we

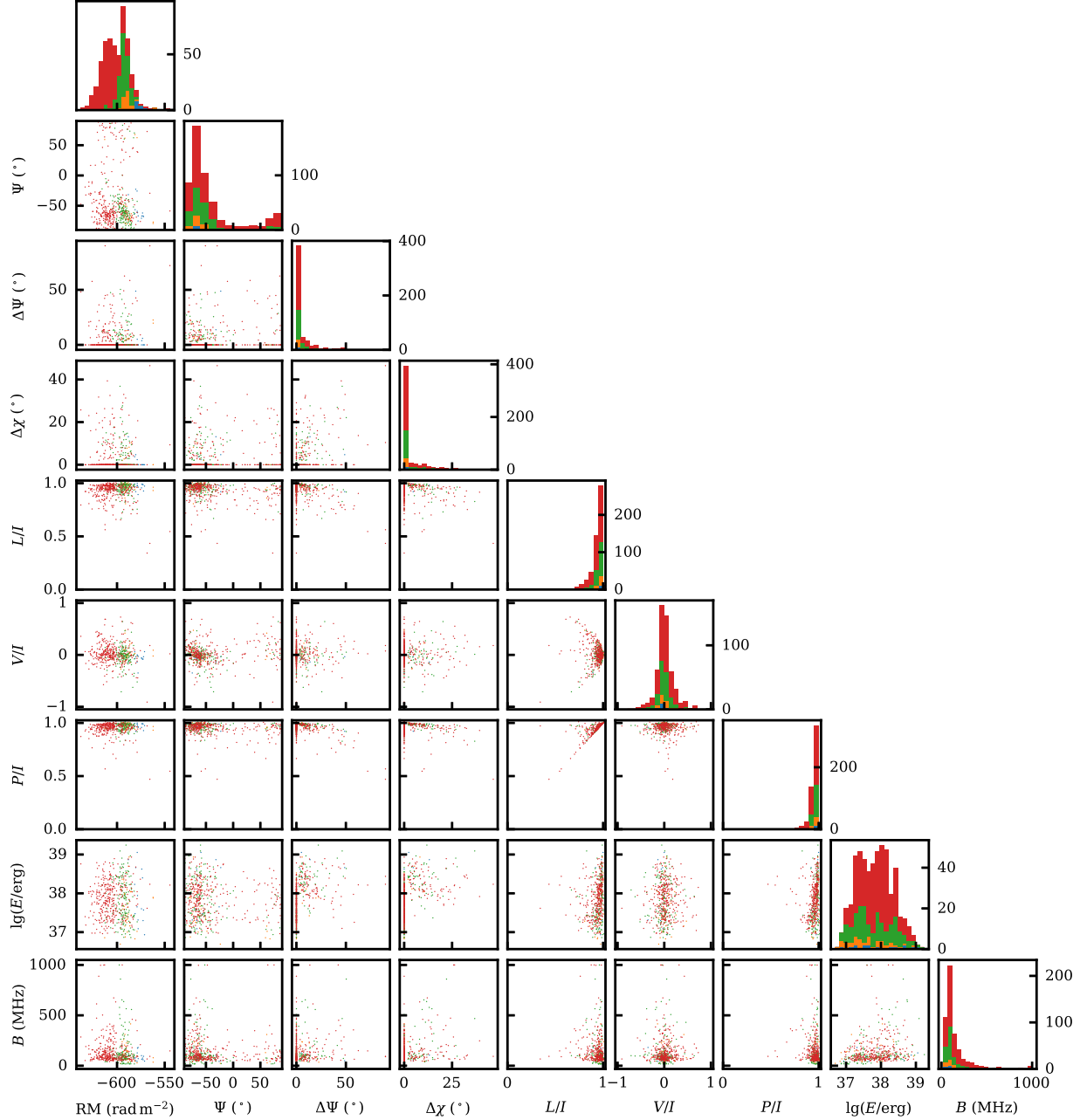


**Figure 3.** The scatterplot matrix of DM, RM, PA  $\Psi$ , maximum change of PA  $\Delta\Psi$ , degree of linear polarization  $L/I$ , degree of circular polarization  $V/I$ , burst energy  $E$  and burst bandwidth  $B$ . Bursts on MJD 59482, 59483, 59484 and 59485 are marked in blue, orange, green and red respectively.

cannot conclude if the averages or the widths of bandwidth and energy have changed in our four-day observations.

To understand the physics behind the temporal evolution of parameter distributions, we investigate the correlation between parameter pairs as depicted in Figure 3. The zoomed-in version is available in Appendix F. For bursts with no obvious (less than  $5\sigma$ )  $\Delta\Psi$  or  $\Delta\chi$ , we plot them with  $\Delta\Psi = 0$  or  $\Delta\chi = 0$ , which form line-like artificial structures in the plots. We see

clear correlations induced by the parameter dependence, i.e.,  $L/I$ - $V/I$ ,  $L/I$ - $P/I$  and energy-bandwidth. Here, the  $L/I$ - $V/I$  and  $L/I$ - $P/I$  correlations come from the definition of the total polarization ( $P^2 \equiv L^2 + V^2$ ), and the fact that total polarization is less than the intensity ( $P/I \leq 1$ ).

No obvious correlation is found between the RM and the PA  $\Psi$ . In this way, we conclude that (1) RM change was not caused by the change in  $\Psi$ ; and (2) the  $\Psi$  distribution was intrinsic and

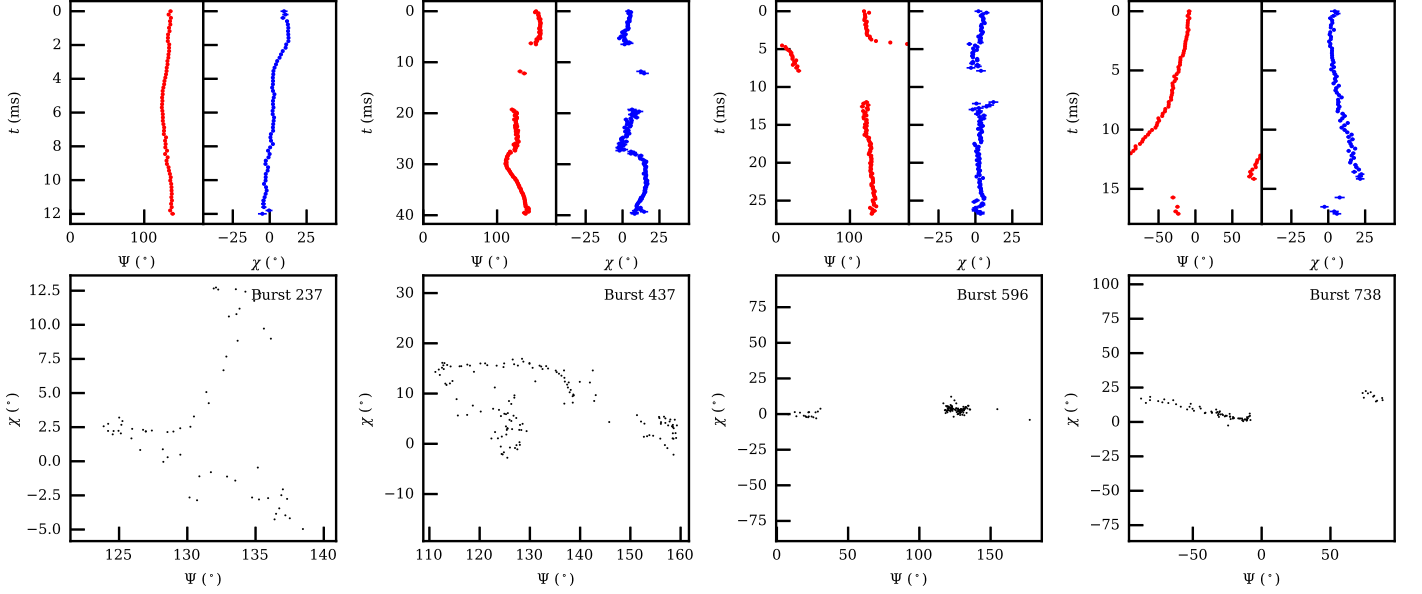


**Figure 4.**  $\Psi$  and  $\chi$  curves of four bursts. (a) The curve of PA  $\Psi$ . (b) The curve of ellipticity angle  $\chi$ . (c) Correlation between  $\Psi$  and  $\chi$  curves. Error bars in (a) and (b) signify 68% confidence level.

not induced by fluctuations in RM. We can attribute the RM change to the FRB environment and  $\Psi$  distribution to the FRB intrinsic properties. A self-consistent picture would be that (1) the magnetoionic environment of the FRB is highly variable to produce RM variations, while (2) the geometric center of the emission region is kept constant to produce a stable average value of  $\Psi$ . At the same time, (3) the spatial size of the emission region is growing larger to produce the increasing fluctuations in the  $\Psi$  distribution.

There may be marginal correlations between parameter pairs of  $\Delta\Psi-L/I$ ,  $\Delta\Psi-P/I$ ,  $\Delta\chi-L/I$  and  $\Delta\chi-P/I$ . Those correlations are expected, since the degree of linear polarization would decrease, if the variation of the PA increases, i.e., degree of polarization would decrease if one adds up radiation with different PAs.

There is a weak  $\Delta\Psi-\Delta\chi$  correlation (see Figure F5), where the correlation coefficient is  $\rho=0.45$  after excluding points with  $\Delta\Psi=0$  and  $\Delta\chi=0$ . This indicates polarization dependent radiative transfer, in which Stokes parameters can convert from one to another.<sup>21</sup> We investigate the phenomenon by checking the phase-resolved relation between the two parameters as displayed in Figure 4 (more examples are given in Appendix G). We can see the correlation between  $\Psi$  and  $\chi$  along the burst time and clear patterns in the trajectories of phase-resolved polarization profile on the surface of the Poincaré sphere (panel (c) of Figure 4). The polarization trajectories exhibit a great diversity. They can be a

straight line or a single curve (Burst 738), or a curve with branches (Burst 237), or a more complex shape (Burst 437). If such trajectories were generated at the pulse emission stage, a complex geometry for the magnetospheric magnetic fields is required. On the other hand, if it is due to polarization radiative transfer, we expect that the magnetic field in the plasma medium is time dependent and also follows a non-simple geometric configuration.

Certain aspects of the polarization behaviors can be understood within the scenario of bunched coherent curvature radiation, which allows for a diversity in polarization. The charged bunches can produce considerably circular polarization, when the line of sight sweeps across the rim of the radiation beam (the angular size  $\sim 1/\gamma$ ); while emissions are strongly linearly polarized, when the opening angle of the bunch is much larger than  $1/\gamma$  (Wang et al. 2022b). Furthermore, different kinds of evolutionary trajectories can be reproduced on the Poincaré sphere (Wang et al. 2022a). Our results suggest that most bunches have large opening angles to produce a high degree of linear polarization, while a small fraction of the bunches have smaller opening angles and display an off-axial generation of radio waves.

## 5. Conclusions

In this manuscript, we presented the statistical results of FAST polarimetric observations of FRB 20201124A from 2021 September 25 to 28. We also compared the current results with the previous observations carried out half a year ago. We

<sup>21</sup> For interested readers, the polarization dependent radiative transfer in the context of FRB is addressed in Xu et al. (2022), which includes the Faraday conversion discussed later in Kumar et al. (2022a).



detected RM evolution and pulse-to-pulse RM scatter with properties similar to previous results.

We note that the diversity in the burst polarization properties is similar to the case of radio pulsars, which disfavors the relativistic shock-wave models for FRBs and provides further evidence for the magnetospheric origin of FRBs. The most-probable values of the polarization degrees, i.e.,  $V/I$ ,  $L/I$  and  $P/I$ , are stable throughout the observation period, but the values are slightly higher than those seen a couple of months ago. We note that the distribution of the polarization degrees is more scattered than that of the March to May session.

We have excluded the hypothesis that the RM variations cause the evolution of the polarization properties, and we are able to isolate the environmental contribution from the FRB intrinsic evolution. The distributions of the PA and polarization degrees evolved toward a more scattered state within the four-day window. We argue that the phenomena are caused by the expansion of the size of the radiation region in the magnetosphere.

We found a weak correlation between the PA variation and the ellipticity angle variation. Such a correlation, together with the complex trajectories of the polarization profiles in the Poincaré sphere representation, suggests that polarization dependent radiative transfer plays a significant role in shaping the polarization properties of FRBs.

We note that the ellipticity angle variation is correlated with the burst energy. So far, there is no theoretical prediction or explanation for this correlation. We expect that a future collection of a larger sample of FRB 20201124A may help to identify or falsify such a correlation. Investigations of the circular polarization properties of some bursts may help to understand the radiation mechanism of FRBs and the immediate environment of the FRB source through propagation effects.

### Acknowledgments

We thank the anonymous referee for providing valuable suggestions. This work made use of the data from FAST (Five-hundred-meter Aperture Spherical radio Telescope). FAST is a Chinese national mega-science facility, operated by National Astronomical Observatories, Chinese Academy of Sciences. This work is supported by the National SKA Program of China (2020SKA0120100, 2020SKA0120200), the National Key R&D Program of China (2017YFA0402602), the National Natural Science Foundation of China (NSFC, Grant No. 12041303), the CAS-MPG LEGACY project and funding from the Max-Planck Partner Group. J.L. Han is supported by the National Natural Science Foundation of China (NSFC, Grant Nos. 11988101 and 11833009) and the Key Research Program of the Chinese Academy of Sciences (Grant No. QYZDJ-SSW-SLH021); D.J. Zhou is supported by the Cultivation Project for the FAST scientific Payoff and Research Achievement of CAMS-CAS. Y. Feng is supported by the Key Research Project of Zhejiang Lab

no. 2021PE0AC0. Y.P.Y. is supported by National Natural Science Foundation of China (Grant No. 12003028) and the China Manned Space Project (CMS-CSST-2021-B11).

### Authors Contributions

J. C. Jiang, K. J. Lee and B. Zhang led the charge of writing this paper and performed the polarimetry and data analysis in this paper. B. Zhang initially proposed the FRB key science project. B. Zhang, K. J. Lee, J. L. Han, W. W. Zhu and D. Li coordinated the teamwork, the observational campaign, and co-supervised data analyses and interpretations. W. Y. Wang, K. J. Lee, D. Z. Li, R. X. Xu and Y. P. Yang provided theoretical inputs. D. J. Zhou studied burst morphology and classification with the details presented in Paper I of this series. Y. K. Zhang analyzed the energy distribution with the details presented in Paper II of this series. J. R. Niu performed periodicity search with the results presented in Paper IV. H. Xu, J. W. Xu, C. F. Zhang, B. J. Wang, D. J. Zhou, Y. Feng, W. C. Jing, R. Luo, C. C. Miao, C. H. Niu, P. Wang, Z. L. Yang and M. Yuan did the data analysis. Z. G. Dai, J. M. Yao, C. W. Tsai and F. Y. Wang participated in the joint discussion.

### Appendix A

#### FAST Polarimetric Test at Large Zenith Angles

The active reflector of FAST consists of 4450 movable reflective panels, which are controlled by actuators to form the instantaneous 300 m aperture parabolic surface from a 500 m aperture spherical surface (Jiang et al. 2019). When the zenith angle reaches  $26^\circ.4$ , the edge of the paraboloid reaches the edge of the spherical reflector and the paraboloid becomes asymmetric. Such a large-angle illumination generates systematic error in polarimetry. In addition, the receiver is tilted back toward the reflector surface to avoid stray illumination coming out of the reflector. The asymmetric reflector and tilted feed illumination generate the beam squint effect (Robshaw & Heiles 2021), therefore we test polarimetric properties for a large zenith angle observation.

The trajectory of FRB 20201124A in FAST sky coverage is drawn in Figure A1. At the start of the observation on September 27 (MJD 59484) and most part of the observation on September 28 (MJD 59485), the zenith angles of the source exceeded the  $26^\circ.4$  limit of full reflector illumination.<sup>22</sup>

In order to test FAST polarimetry at large zenith angles ( $>26^\circ.4$ ), we utilized archival data of Chinese Pulsar Timing Array (CPTA) (Lee 2016) and compared the polarimetric results of PSR J0621+1002 at zenith angles smaller and larger than  $26^\circ.4$ . The test data were obtained between July 2019 and August 2021; 35 observations of PSR J0621+1002 were conducted at small zenith angles ( $<26^\circ.4$ ), but the zenith angle of one observation on 2020 July 30 (MJD 59060) was

<sup>22</sup> <https://fastwww.china-vo.org/cms/article/24/>

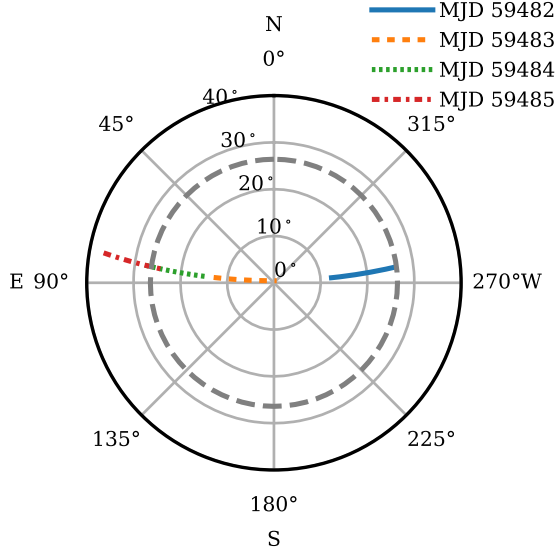


**Figure A1.** Horizontal coordinates of FRB 20201124A in FAST observations between September 26 (MJD 59482) and 29 (MJD 59485). In the polar plot, the polar angle is the azimuth angle, and the distance is the zenith angle of the source. The dashed gray circle signifies the  $26.4^\circ$  limit between small and large zenith angles of FAST. At the start of the observation on September 28 (MJD 59484) and most part of the observation on September 29 (MJD 59485), the zenith angles of the source exceeded the limit.

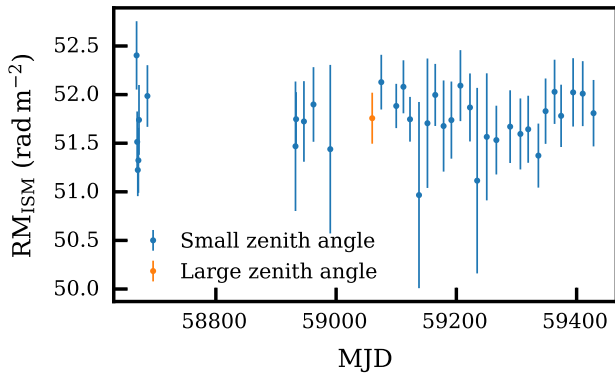


**Figure A2.** RMs of PSR J0621+1002 in CPTA data. The contribution of the ionosphere of the Earth has been subtracted. The blue marks correspond to observations at small zenith angles ( $<26.4^\circ$ ), while the orange mark represents the observation at large zenith angle. Error bars signify 68% confidence level.

between  $29.5^\circ$  and  $35.7^\circ$ . We followed a phase-resolved Bayesian method to fit  $RM_{\text{obs}}$  of all observations, and subtracted RM of the ionosphere of the Earth  $RM_{\text{ion}}$  using  $\text{ionFR}^{23}$  (Sotomayor-Beltran et al. 2013) to get the RM of interstellar medium  $RM_{\text{ISM}}$ . The results in Figure A2 demonstrate that RM is not affected at the level of  $0.3 \text{ rad m}^{-2}$  in the large-angle observation.

<sup>23</sup> <https://sourceforge.net/projects/ionfarrot/>

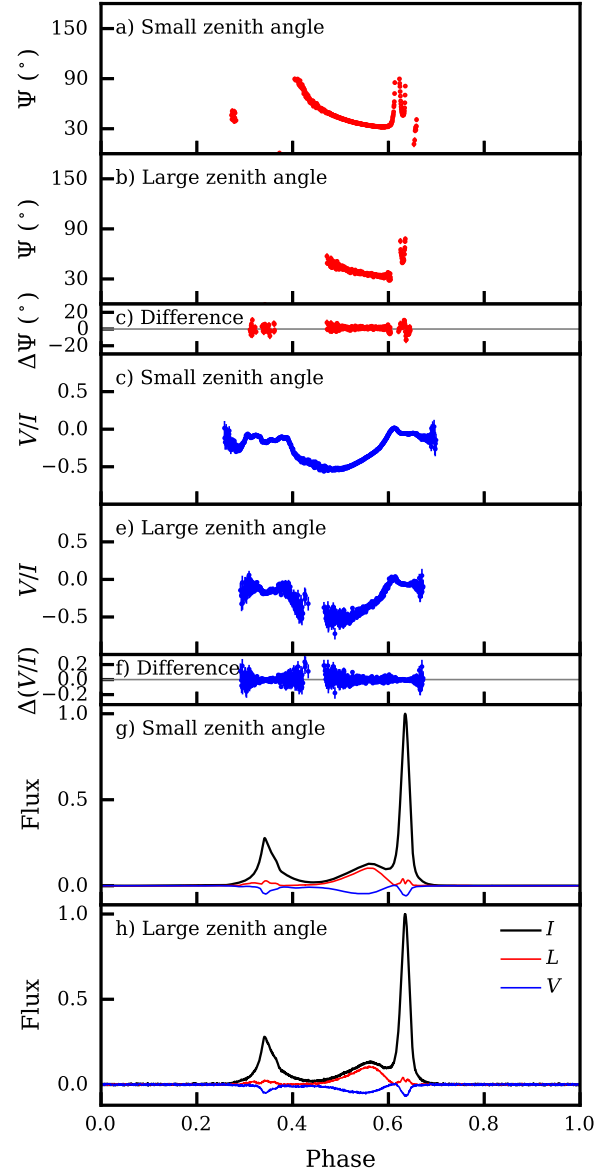


**Figure A3.** Polarimetric results of PSR J0621+1002. (a) PA  $\Psi$  at small zenith angle. (b) PA  $\Psi$  at large zenith angle. (c) Differences in PA  $\Psi$  between large and small zenith angle. (d) Degree of circular polarization  $V/I$  at small zenith angle. (e) Degree of circular polarization  $V/I$  at large zenith angle. (f) Differences in degree of circular polarization  $V/I$  between large and small zenith angle. (g) Polarization profiles at small zenith angle. (h) Polarization profiles at large zenith angle. Profiles in Panels (g) and (h) are normalized by the peak of total intensity  $I$ . The black curve is total intensity  $I$ , the red curve is linearly polarized intensity  $L$  and the blue curve is circularly polarized intensity  $V$ . Error bars in Panels (a) to (f) signify 68% confidence level.

We also combined the polarization profiles of small zenith angle observations after correcting Faraday rotation using  $RM_{\text{obs}}$  of each observation, and compared the combined profile with the polarization profile at large zenith angle. The results displayed in Figure A3 show no significant difference in polarization profiles except S/N because the total observation

time at small zenith angle was much longer than the observation at large zenith angle. The differences in PA between the observations of large and small zenith angles were  $1.4 \pm 0.8$ . For the degree of circular polarization  $|V|/I$ , the result of combined small zenith angle observations is  $(16.282 \pm 0.010)\%$ , and the result of the large zenith angle observation is  $(16.92 \pm 0.07)\%$ , therefore the systematic error of  $|V|/I$  is less than 1%. We conclude that at the 1% level, the polarimetry is not affected by the large-angle illumination.

## Appendix B Measure RM

When a linearly polarized radio wave propagates in the cold magnetized plasma, the plane of polarization rotates. Such rotation is called Faraday rotation. The angle of polarization plane, i.e., the PA  $\Psi$ , is wavelength ( $\lambda$ ) dependent such that

$$\Delta\Psi = \text{RM} \lambda^2, \quad (\text{B1})$$

where the coefficient RM is the Faraday RM. We used a Bayesian method (Desvignes et al. 2019; Luo et al. 2020) to fit the rotation in terms of Stokes  $Q$  and  $U$  of the burst to obtain the RM. The best fit value and uncertainty interval for the RM of each burst were derived from the posterior inference using `PyMultiNest`<sup>24</sup> (Buchner et al. 2014). More details of the fitting method can be found in the Supplementary Materials of Desvignes et al. (2019). The ionosphere of the Earth also contributes to the observed RMs. Software package `ionFR`<sup>25</sup> (Sotomayor-Beltran et al. 2013) was employed to correct the RM contribution due to the ionosphere and geomagnetic field. The results are depicted in Figure B1.

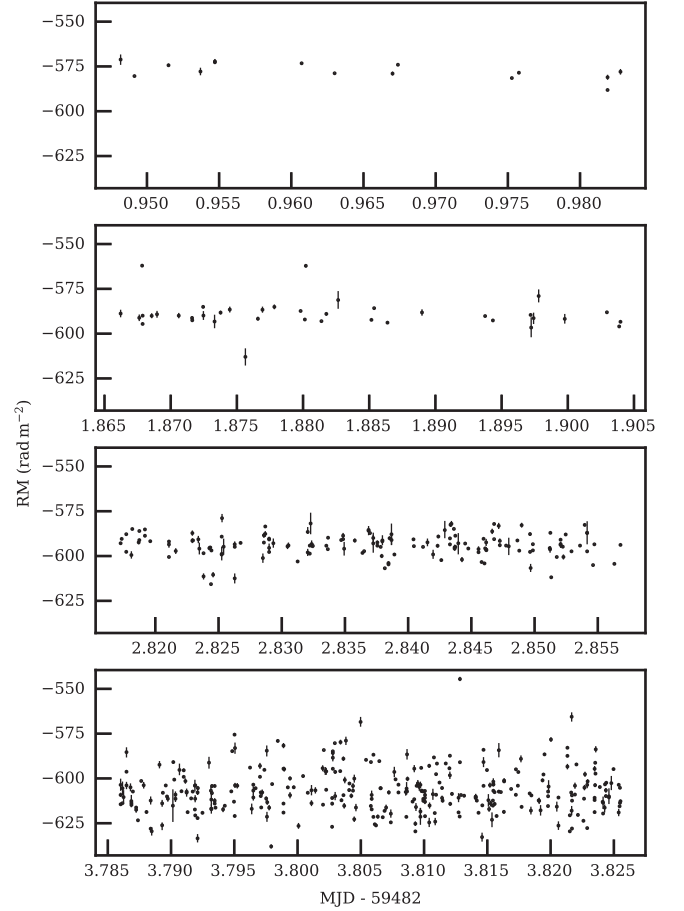


**Figure B1.** Example of fitted RMs for bursts in September 2021. The error bars signify 68% confidence intervals. Four panels are used to show observing sessions.

<sup>24</sup> <https://johannesbuchner.github.io/PyMultiNest/>

<sup>25</sup> <https://sourceforge.net/projects/ionfarrot/>

### Appendix C Maximal $\Delta\Psi$

The difference of PA  $\Delta\Psi$  can be calculated using Stokes  $Q$  and  $U$

$$\Delta\Psi_{ij} = \frac{1}{2} \arccos D_{\Psi,ij}, \quad (C1)$$

$$D_{\Psi,ij} = \frac{Q_i Q_j + U_i U_j}{\sqrt{(Q_i^2 + U_i^2)(Q_j^2 + U_j^2)}}, \quad (C2)$$

where subscripts  $i$  and  $j$  denote that  $\Delta\Psi_{ij}$  is the difference of PA between the  $i$ th and the  $j$ th sample of a given pulse profile. The uncertainty in  $\Delta\Psi$  is computed with error propagation formula

$$\sigma_{\Delta\Psi,ij} = \frac{1}{2} \sqrt{\frac{\sigma_{D_{\Psi,ij}}^2}{1 - D_{\Psi,ij}^2}}, \quad (C3)$$

with

$$\sigma_{D_{\Psi,ij}}^2 = \left[ \left( \frac{\partial D_{\Psi}}{\partial Q_i} \right)^2 + \left( \frac{\partial D_{\Psi}}{\partial Q_j} \right)^2 \right] \sigma_Q^2 + \left[ \left( \frac{\partial D_{\Psi}}{\partial U_i} \right)^2 + \left( \frac{\partial D_{\Psi}}{\partial U_j} \right)^2 \right] \sigma_U^2, \quad (C4)$$

and

$$\frac{\partial D_{\Psi}}{\partial Q_i} = \frac{U_i(Q_j U_i - Q_i U_j)}{L_i^3 L_j}, \quad (C5)$$

$$\frac{\partial D_{\Psi}}{\partial Q_j} = \frac{U_j(Q_i U_j - Q_j U_i)}{L_j^3 L_i}, \quad (C6)$$

$$\frac{\partial D_{\Psi}}{\partial U_i} = \frac{Q_i(Q_i U_j - Q_j U_i)}{L_i^3 L_j}, \quad (C7)$$

$$\frac{\partial D_{\Psi}}{\partial U_j} = \frac{Q_j(Q_j U_i - Q_i U_j)}{L_j^3 L_i}. \quad (C8)$$

Here the errors for  $Q$  and  $U$ , i.e.,  $\sigma_Q$  and  $\sigma_U$ , are estimated using the standard deviations of  $Q$  and  $U$  in the off-burst baselines. The maximal PA variation can thus be defined as

$$\Delta\Psi = \max_{\forall i,j \text{ s.t. } \frac{\Delta\Psi_{ij}}{\sigma_{\Delta\Psi,ij}} \geq 5} \Delta\Psi_{ij}. \quad (C9)$$

When condition  $\Delta\Psi/\sigma_{\Delta\Psi} > 5$  could not be met ( $\sim 66\%$  of bursts with  $S/N > 50$ ), we denoted  $\Delta\Psi$  as 0.

### Appendix D Maximal $\Delta\chi$

Similar to the case of PA  $\Delta\Psi$ , the difference in ellipticity angle  $\Delta\chi$  between the  $i$ th and  $j$ th data points is

$$D_{\chi,ij} = \frac{L_i L_j + V_i V_j}{P_i P_j} = \frac{\sqrt{(Q_i^2 + U_i^2)(Q_j^2 + U_j^2)} + V_i V_j}{\sqrt{(Q_i^2 + U_i^2 + V_i^2)(Q_j^2 + U_j^2 + V_j^2)}}, \quad (D1)$$

$$\Delta\Psi_{ij} = \frac{1}{2} \arccos D_{\chi,ij}. \quad (D2)$$

The uncertainty in  $\Delta\chi$  is given by

$$\frac{\partial D_{\chi}}{\partial Q_i} = \frac{Q_i V_i (L_j V_i - L_i V_j)}{L_i P_i^3 P_j}, \quad (D3)$$

$$\frac{\partial D_{\chi}}{\partial Q_j} = \frac{Q_j V_j (L_i V_j - L_j V_i)}{L_j P_j^3 P_i}, \quad (D4)$$

$$\frac{\partial D_{\chi}}{\partial U_i} = \frac{U_i V_i (L_j V_i - L_i V_j)}{L_i P_i^3 P_j}, \quad (D5)$$

$$\frac{\partial D_{\chi}}{\partial U_j} = \frac{U_j V_j (L_i V_j - L_j V_i)}{L_j P_j^3 P_i}, \quad (D6)$$

$$\frac{\partial D_{\chi}}{\partial V_i} = \frac{L_i (L_i V_j - L_j V_i)}{P_i^3 P_j}, \quad (D7)$$

$$\frac{\partial D_{\chi}}{\partial V_j} = \frac{L_j (L_j V_i - L_i V_j)}{P_j^3 P_i}, \quad (D8)$$

$$\sigma_{D_{\chi}}^2 = \left[ \left( \frac{\partial D_{\chi}}{\partial Q_i} \right)^2 + \left( \frac{\partial D_{\chi}}{\partial Q_j} \right)^2 \right] \sigma_Q^2 + \left[ \left( \frac{\partial D_{\chi}}{\partial U_i} \right)^2 + \left( \frac{\partial D_{\chi}}{\partial U_j} \right)^2 \right] \sigma_U^2 + \left[ \left( \frac{\partial D_{\chi}}{\partial V_i} \right)^2 + \left( \frac{\partial D_{\chi}}{\partial V_j} \right)^2 \right] \sigma_V^2, \quad (D9)$$

$$\sigma_{\Delta\chi} = \frac{1}{2} \sqrt{\frac{\sigma_{D_{\chi}}^2}{1 - D_{\chi}^2}}. \quad (D10)$$

The maximal value of  $\Delta\chi$  is

$$\Delta\chi = \max_{\forall i,j \text{ s.t. } \frac{\Delta\chi_{ij}}{\sigma_{\Delta\chi,ij}} \geq 5} \Delta\chi_{ij}. \quad (D11)$$

In our observation, 72% of bursts with  $S/N > 50$  cannot meet the condition  $\Delta\chi/\sigma_{\Delta\chi} > 5$ ; they are marked as  $\Delta\chi = 0$ .

## Appendix E Circular Standard Deviation of Position Angle

Due to a periodic boundary of  $180^\circ$ , the circular standard deviation of PA  $\sigma_\Psi$  is defined as

$$\bar{C} = \frac{1}{N} \sum_{i=0}^{N-1} \cos 2\Psi_i, \quad (\text{E1})$$

$$\bar{S} = \frac{1}{N} \sum_{i=0}^{N-1} \sin 2\Psi_i, \quad (\text{E2})$$

$$\bar{R} = \sqrt{\bar{C}^2 + \bar{S}^2}, \quad (\text{E3})$$

$$\sigma_\Psi = \frac{1}{2} \sqrt{-2 \ln \bar{R}}, \quad (\text{E4})$$

where  $\Psi_i$  is the PA of each burst, and  $N$  is the number of bursts.

The error of  $\sigma_\Psi$  is inferred using the standard re-sampling technique (Efron 1982), where the values of each day are randomly re-sampled without putting back. The circular standard deviation is estimated by re-scaling the post-sampling ensemble standard deviation with the ensemble size factor.

## Appendix F Zoomed-in Correlation Relation

In this section, we collect the zoomed-in version of Figure 3, where the RM- $\Psi$ ,  $L/I$ - $V/I$ ,  $\chi$ - $P/I$ ,  $E$ - $B$  and  $\Delta\Psi$ - $\Delta\chi$  correlations are in Figures F1-F5.

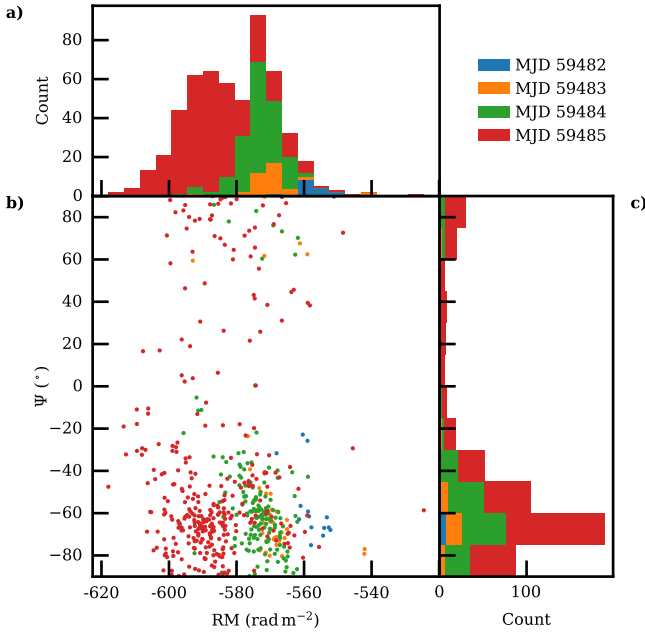


**Figure F1.** (a) Histogram of RM. (b) Correlation between RM and PA. (c) Histogram of PA  $\Psi$ .

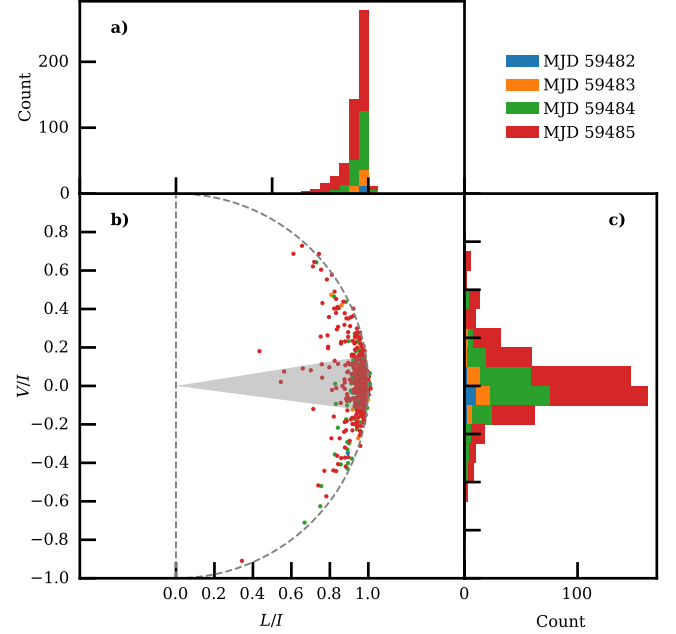


**Figure F2.** (a) Histogram of degree of linear polarization  $L/I$ . (b) Correlation between degree of linear polarization  $L/I$  and degree of circular polarization  $V/I$ . The gray dashed semicircle traces the area in which the degree of polarization  $P/I = \sqrt{L^2 + V^2}/I \leq 1$ . The gray sector covers 68% of bursts. (c) Histogram of degree of circular polarization  $V/I$ .

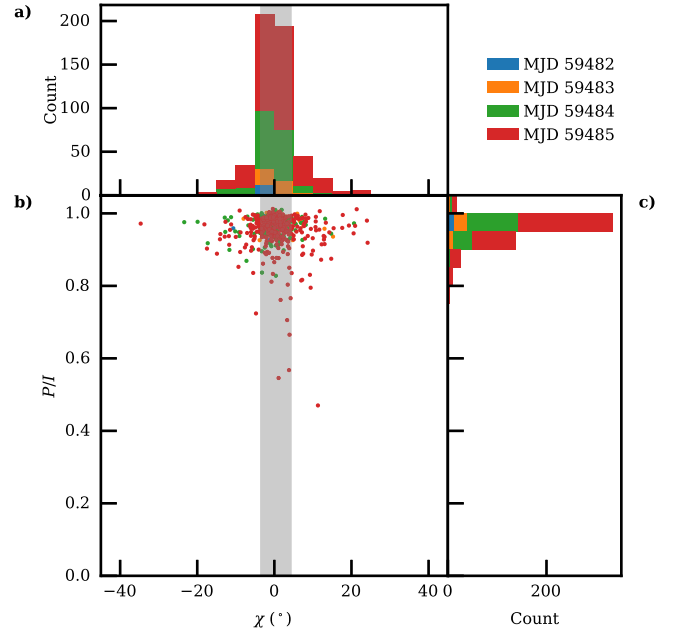


**Figure F3.** (a) Histogram of ellipticity angle  $\chi$ . (b) Correlation between ellipticity angle  $\chi$  and degree of polarization  $P/I$ . (c) Histogram of degree of polarization  $P/I$ . The gray shade covers 68% of bursts.



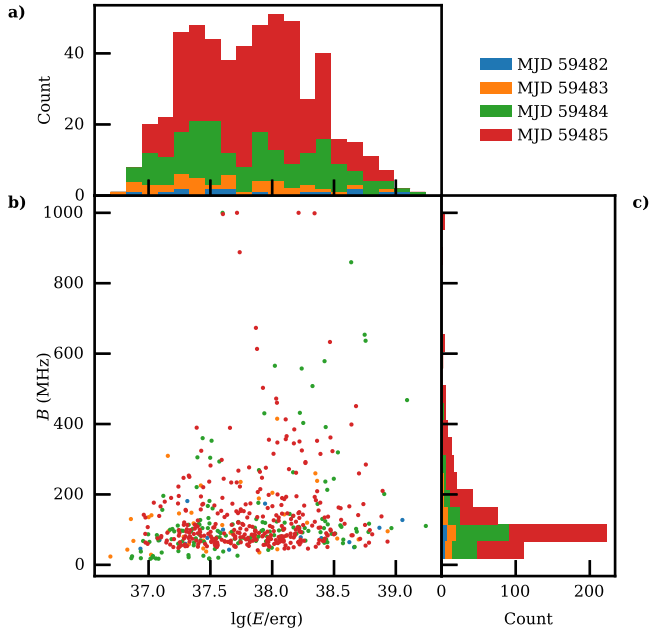


**Figure F4.** (a) Histogram of burst energy  $E$ . (b) Correlation between burst energy  $E$  and burst bandwidth  $B$ . (c) Histogram of burst bandwidth  $B$ .

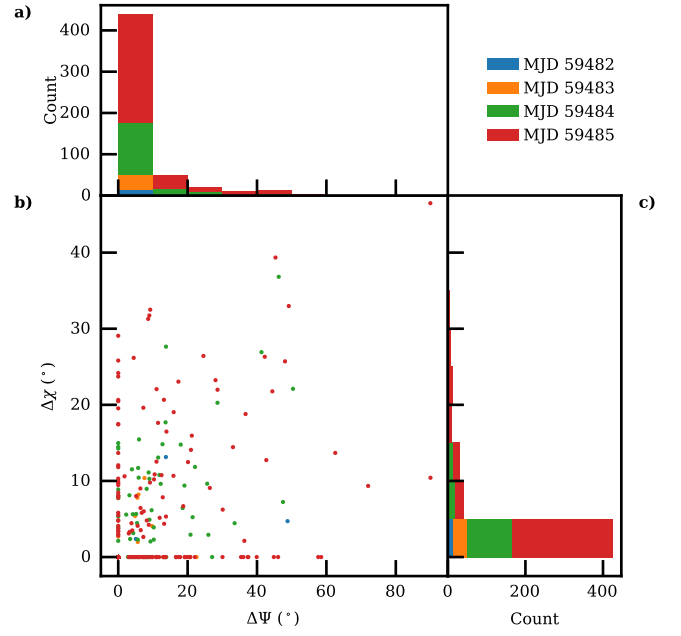


**Figure F5.** (a) Histogram of the maximum change in the PA across the pulse profile  $\Delta\Psi$ . (b) Correlation between  $\Delta\Psi$  and  $\Delta\chi$ . (c) Histogram of the maximum change in the ellipticity angle across the pulse profile  $\Delta\chi$ .

## Appendix G $\Psi$ and $\chi$ Curves

Figure G1 collects the phase resolved  $\Psi$ - $\chi$  curves of all bursts with  $\Delta\Psi > 20^\circ$ ,  $\Delta\chi > 10^\circ$  and  $S/N > 200$ .

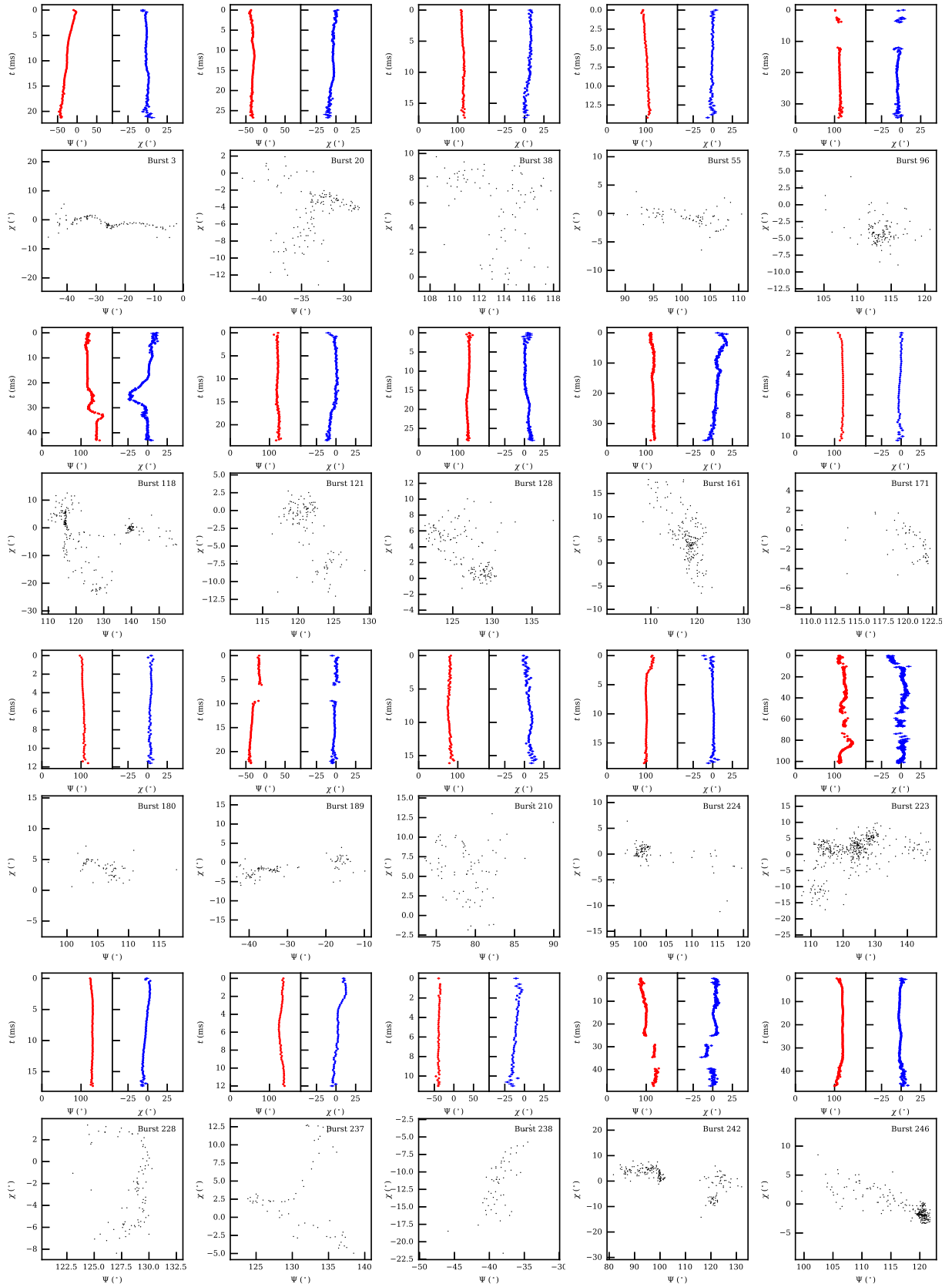


**Figure G1.**  $\Psi$  and  $\chi$  curves of all bursts with  $\Delta\Psi > 20^\circ$ ,  $\Delta\chi > 10^\circ$  and S/N > 200. The symbols and colors are the same as those in Figure 4.

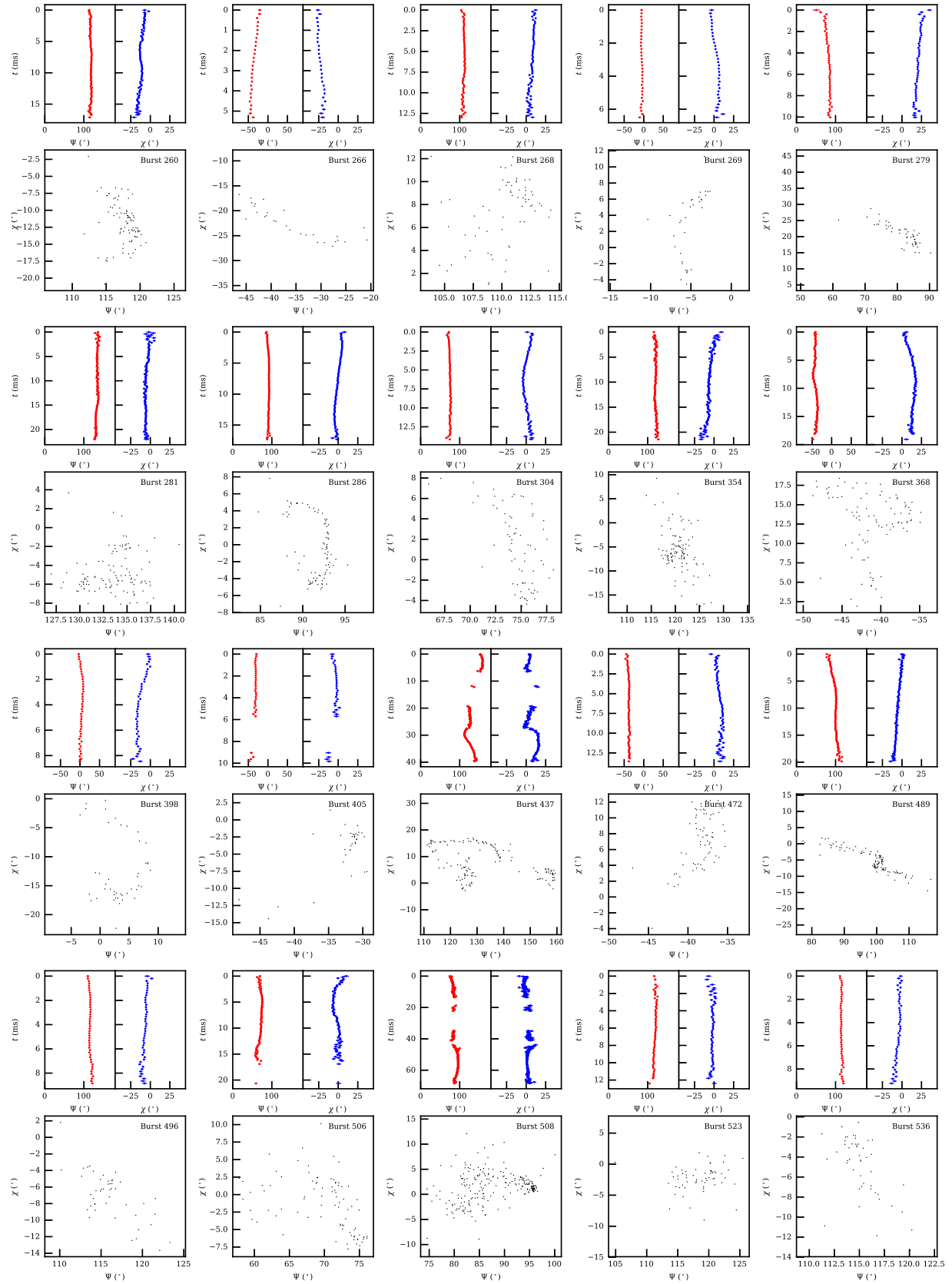


Figure G1. (Continued.)

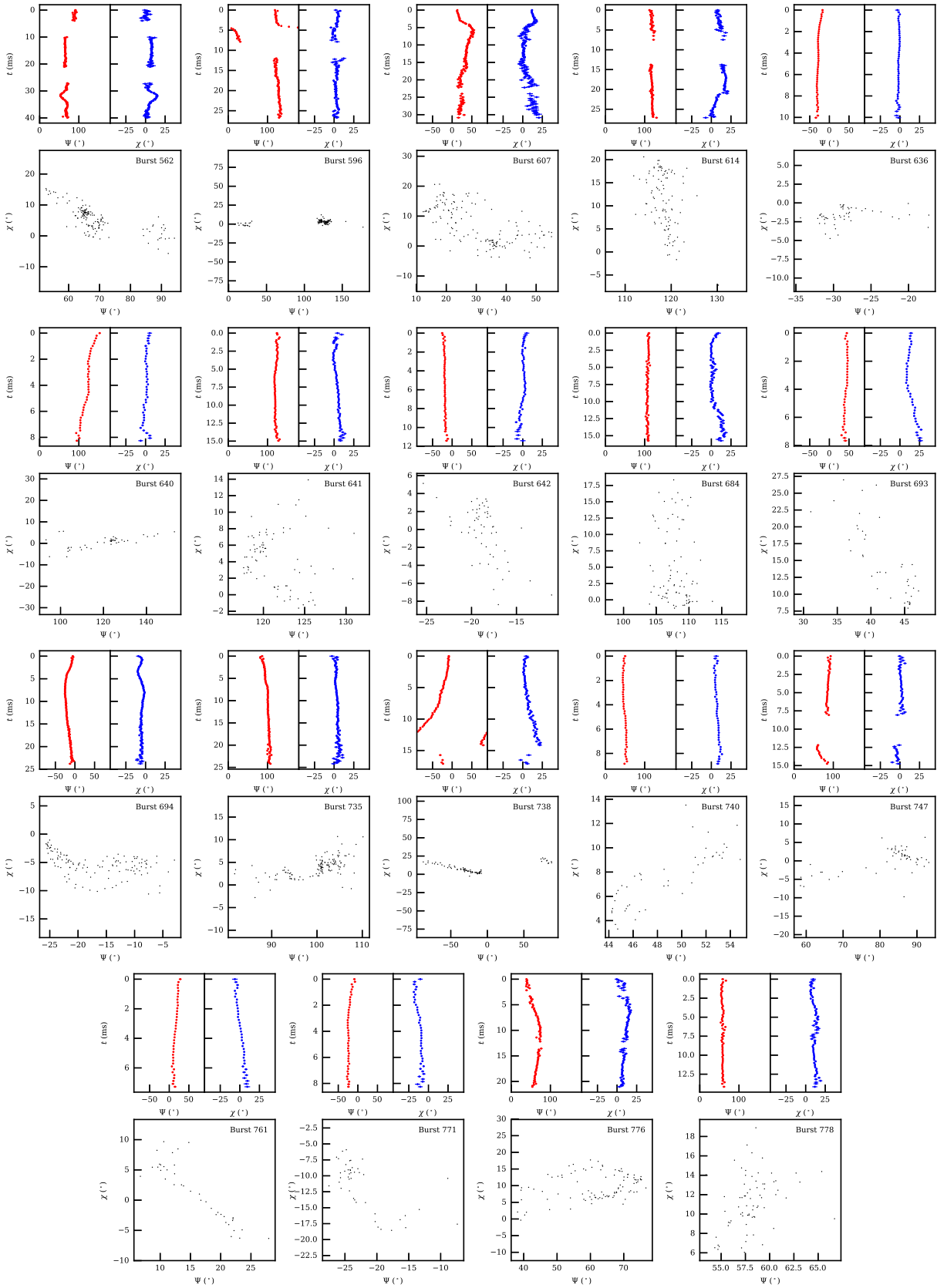


Figure G1. (Continued.)

## ORCID iDs

Jin-Chen Jiang  <https://orcid.org/0000-0002-6465-0091>  
 De-Jiang Zhou  <https://orcid.org/0000-0002-6423-6106>  
 Yong-Kun Zhang  <https://orcid.org/0000-0002-8744-3546>  
 Jia-Rui Niu  <https://orcid.org/0000-0001-8065-4191>  
 Wei-Cong Jing  <https://orcid.org/0000-0002-1056-5895>  
 Rui Luo  <https://orcid.org/0000-0002-4300-121X>

## References

- Anna-Thomas, R., Connor, L., Burke-Spolaor, S., et al. 2022, arXiv:2202.11112
- Beloborodov, A. M. 2020, *ApJ*, **896**, 142
- Beniamini, P., Kumar, P., & Narayan, R. 2022, *MNRAS*, **510**, 4654
- Buchner, J., Georgakakis, A., Nandra, K., et al. 2014, *A&A*, **564**, A125
- Chawla, P., Andersen, B. C., Bhardwaj, M., et al. 2020, *ApJL*, **896**, L41
- CHIME/FRB Collaboration 2021, ATel, 14497, 1
- CHIME/FRB Collaboration, Andersen, B. C., Bandura, K., et al. 2019, *ApJL*, **885**, L24
- Dai, S., Feng, Y., Yang, Y. P., et al. 2022, arXiv:2203.08151
- Day, C. K., Deller, A. T., Shannon, R. M., et al. 2020, *MNRAS*, **497**, 3335
- Desvignes, G., Kramer, M., Lee, K., et al. 2019, *Sci*, **365**, 1013
- Dunning, A., Bowen, M., Castillo, S., et al. 2017, in 2017 32nd General Assembly and Scientific Symposium of the Int. Union of Radio Science (URSI GASS) (19–26 August 2017) (Montreal, QC: IEEE), 1
- Efron, B. 1982, in The Jackknife, the Bootstrap and Other Resampling Plans (Philadelphia, PA: Society for Industrial and Applied Mathematics (SIAM))
- Everett, J. E., & Weisberg, J. M. 2001, *ApJ*, **553**, 341
- Faber, J. T., Gajjar, V., Siemion, A. P. V., et al. 2021, *RNAAS*, **5**, 17
- Feng, Y., Li, D., Yang, Y.-P., et al. 2022, *Sci*, **375**, 1266
- Fisher, N. I. 1996, *Statistical Analysis of Circular Data* (Cambridge: Cambridge Univ. Press)
- Fonseca, E., Andersen, B. C., Bhardwaj, M., et al. 2020, *ApJL*, **891**, L6
- Gajjar, V., Siemion, A. P. V., Price, D. C., et al. 2018, *ApJ*, **863**, 2
- Hilmarsson, G. H., Michilli, D., Spitler, L. G., et al. 2021a, *ApJL*, **908**, L10
- Hilmarsson, G. H., Spitler, L. G., Main, R. A., & Li, D. Z. 2021b, *MNRAS*, **508**, 5354
- Hobbs, G. 2012, arXiv:1205.6273
- Hobbs, G., & Edwards, R. 2012, Tempo2: Pulsar Timing Package, <https://bitbucket.org/psrsoft/tempo2/src/master/>
- Hobbs, G. B., Edwards, R. T., & Manchester, R. N. 2006, *MNRAS*, **369**, 655
- Hotan, A. W., van Straten, W., & Manchester, R. N. 2004, *PASA*, **21**, 302
- Huang, L., & Shcherbakov, R. V. 2011, *MNRAS*, **416**, 2574
- Jiang, P., Tang, N.-Y., Hou, L.-G., et al. 2020, *RAA*, **20**, 064
- Jiang, P., Yue, Y., Gan, H., et al. 2019, *SCPMA*, **62**, 959502
- Kumar, P., & Bošnjak, Ž. 2020, *MNRAS*, **494**, 2385
- Kumar, P., Shannon, R. M., Flynn, C., et al. 2021, *MNRAS*, **500**, 2525
- Kumar, P., Shannon, R. M., Lower, M. E., Deller, A. T., & Prochaska, J. X. 2022a, arXiv:2204.10816
- Kumar, P., Shannon, R. M., Lower, M. E., et al. 2022b, *MNRAS*, **512**, 3400
- LANMAN, A. E., ANDERSEN, B. C., CHAWLA, P., et al. 2022, *ApJ*, **927**, 59
- Lee, K. J. 2016, in ASP Conf. Ser. 502, *Frontiers in Radio Astronomy and FAST Early Sciences Symp.* 2015, ed. L. Qain & D. Li (San Francisco, CA: ASP), 19
- Li, D., Wang, P., Qian, L., et al. 2018, *IMMag*, **19**, 112
- Li, D., Wang, P., Zhu, W. W., et al. 2021, *Natur*, **598**, 267
- Lu, W., Kumar, P., & Zhang, B. 2020, *MNRAS*, **498**, 1397
- Luo, R., Wang, B. J., Men, Y. P., et al. 2020, *Natur*, **586**, 693
- Marcote, B., Kirsten, F., Hessels, J. W. T., et al. 2021, ATel, 14603, 1
- Margalit, B., Beniamini, P., Sridhar, N., & Metzger, B. D. 2020, *ApJL*, **899**, L27
- Men, Y. P., Luo, R., Chen, M. Z., et al. 2019, *MNRAS*, **488**, 3957
- Metzger, B. D., Margalit, B., & Sironi, L. 2019, *MNRAS*, **485**, 4091
- Michilli, D., Seymour, A., Hessels, J. W. T., et al. 2018, *Natur*, **553**, 182
- Nimmo, K., Hessels, J. W. T., Keimpema, A., et al. 2021, *NatAs*, **5**, 594
- Nimmo, K., Hewitt, D. M., Hessels, J. W. T., et al. 2022, *ApJL*, **927**, L3
- Niu, C. H., Aggarwal, K., Li, D., et al. 2022, *Natur*, **606**, 873
- Niu, J., Zhu, W., Zhang, B., et al. 2022, *RAA*, **22**, 124004
- Pastor-Marazuela, I., Connor, L., van Leeuwen, J., et al. 2021, *Natur*, **596**, 505
- Pedregosa, F., Varoquaux, G., Gramfort, A., et al. 2011, *JMLR*, **12**, 2825
- Plavin, A., Paragi, Z., Marcote, B., et al. 2022, *MNRAS*, **511**, 6033
- Pleunis, Z., Michilli, D., Bassa, C. G., et al. 2021, *ApJL*, **911**, L3
- Price, D. C., Foster, G., Geyer, M., et al. 2019, *MNRAS*, **486**, 3636
- Robishaw, T., & Heiles, C. 2021, The measurement of polarization in radio astronomy, in *The WSPC Handbook of Astronomical Instrumentation*, ed. A. Wolszczan (Singapore: World Scientific), 127
- Sand, K. R., Faber, J. T., Gajjar, V., et al. 2022, *ApJ*, **932**, 98
- Sotomayor-Beltran, C., Sobey, C., Hessels, J. W. T., et al. 2013, *A&A*, **552**, A58
- Spitler, L. G., Cordes, J. M., Hessels, J. W. T., et al. 2014, *ApJ*, **790**, 101
- Spitler, L. G., Scholz, P., Hessels, J. W. T., et al. 2016, *Natur*, **531**, 202
- Stinebring, D. R., Cordes, J. M., Rankin, J. M., Weisberg, J. M., & Boriakoff, V. 1984, *ApJS*, **55**, 247
- van Straten, W., & Bailes, M. 2011, *PASA*, **28**, 1
- van Straten, W., Demorest, P., & Osłowski, S. 2012, *AR&T*, **9**, 237
- van Straten, W., Manchester, R. N., Johnston, S., & Reynolds, J. E. 2010, *PASA*, **27**, 104
- Wang, W.-Y., Jiang, J.-C., Lu, J., et al. 2022a, *SCPMA*, **65**, 289511
- Wang, W.-Y., Xu, R., & Chen, X. 2020, *ApJ*, **899**, 109
- Wang, W.-Y., Yang, Y.-P., Niu, C.-H., Xu, R., & Zhang, B. 2022b, *ApJ*, **927**, 105
- Xu, H., Niu, J. R., Chen, P., et al. 2022, *Natur*, **609**, 685
- Yang, Y.-P., Lu, W., Feng, Y., Zhang, B., & Li, D. 2022, *ApJL*, **928**, L16
- Yang, Y.-P., & Zhang, B. 2021, *ApJ*, **919**, 89
- Zhang, B. 2022, *ApJ*, **925**, 53
- Zhang, C. F., Xu, J. W., Men, Y. P., et al. 2021, *MNRAS*, **503**, 5223
- Zhang, Y., Wang, P., Feng, Y., et al. 2022, *RAA*, **22**, 124002
- Zhou, D.-J., Han, J.-L., Zhang, B., et al. 2022, *RAA*, **22**, 124001